Mikailalsys Journal of Advanced Engineering International

e-ISSN : 3046-9694
p-ISSN : 3046-8914

Index : Harvard, Boston, Sydney University, Dimensions, Lens, Scilit, Semantic, Google, etc

https://doi.org/10.58578/MJAEI.v3i3.10169

Energy-Efficient Molten-Salt-Shielded Synthesis of Ti3C2Tx MXene from Low-Cost Precursors and Its Integration into a Carbonized Luffa Sponge Composite for High-Performance Solar-Driven Interfacial Evaporation and Desalination

Mohammed Muktar Nono[1], Idris Misau Muhammad[2], Abdulrahman A. Abdulrasheed[3], Usman Dadum Hamza[4], Prashobh Karunakaran[5]

[1,5]University of Technology Sarawak Sibu, Malaysia

[2,3,4]Abubakar Tafawa Balewa University, Bauchi State, Nigeria

muktarn@fuwukari.edu.ng

Article Info:

Submitted:	Revised:	Accepted:	Published:
Jun 11, 2026	Aug 8, 2026	Aug 20, 2026	Aug 25, 2026

Abstract

Scalable, energy-passive desalination technologies are urgently needed to address the growing freshwater crisis, particularly in off-grid and resource-constrained communities. This study develops an integrated materials pathway spanning the energy-efficient synthesis of $Ti_3C_2T_x$ MXene from low-cost precursors to its application in a high-performance solar desalination platform. The Ti_3AlC_2 MAX phase was synthesized at 1100°C through a molten-salt-shielding synthesis (MS3) route using titanium dioxide (TiO_2), aluminum, and activated carbon in a NaCl–KCl eutectic medium with a 7:3 salt-to-precursor ratio, reducing the synthesis temperature by approximately 600°C relative to conventional solid-state routes. Selective HF/HCl etching subsequently converted the MAX phase into multilayer $Ti_3C_2T_x$ MXene. Successful conversion was confirmed by a characteristic (002) diffraction shift to 7°, accordion-like morphology,

MJAEI Journal is licensed under a Creative Commons Attribution-NonCommercial-ShareAlike 4.0 International License

disappearance of Al–C bonds, and a localized surface plasmon resonance peak at 792 nm. The MXene was deposited onto a carbonized luffa sponge (CLS) through controlled dip coating to produce an MC-CLS photothermal evaporator. Characterization revealed uniform MXene coverage, broadband solar absorptance of ≥0.95 across 200–1100 nm, retained hydrophilic surface terminations, and substantially enhanced thermal stability. Under one-sun illumination (1 kW m^{-2}), MC-CLS achieved an average evaporation rate of 2.12 kg m^{-2} h^{-1} and a solar-to-steam conversion efficiency of 95%. The evaporation rate increased near-linearly to 7.79 kg m^{-2} h^{-1} at 5 kW m^{-2}, while the evaporator retained more than 94% of its performance after 21 wetting–drying cycles. Inductively coupled plasma optical emission spectrometry further confirmed that condensate produced from simulated seawater consistently met World Health Organization drinking-water standards for Na^{+}, K^{+}, Ca^{2+}, and Mg^{2+}. These findings establish an integrated pathway from low-cost MXene synthesis to solar water purification, offering a promising approach to scalable, durable, and energy-autonomous freshwater production.

Keywords: Interfacial Solar Evaporation; Luffa Sponge; Molten-Salt Synthesis; MXene; Solar Desalination

Introduction

Access to clean freshwater is a fundamental prerequisite for human health; however, over two billion people currently live under conditions of high water stress, a figure projected to worsen substantially as global population growth, urbanization, and climate-induced hydrological disruptions accelerate (Boretti & Rosa, 2019; Ingrao et al., 2023). Although seawater and brackish groundwater are vastly abundant alternative sources, their conversion into potable water through conventional technologies, such as reverse osmosis (RO), multi-effect distillation (MED), and multi-stage flash (MSF), is constrained by high energy consumption, dependence on fossil-fuel-powered infrastructure, complex operational requirements, and environmental burdens arising from brine discharge and greenhouse gas emissions (Shokri & Fard, 2022; Tayeh, 2024). These systemic limitations are particularly acute in remote, off-grid, and resource-limited communities, where energy costs and infrastructure barriers render conventional desalination economically inaccessible.

Solar-driven desalination has emerged as a compelling sustainable alternative that harnesses globally abundant and free solar resources. Among solar desalination strategies, interfacial solar steam generation (ISSG) has attracted exceptional research attention because

it localizes thermal energy at the water–air interface, thereby circumventing the large thermal losses inherent to bulk water heating in conventional solar stills (Zhou et al., 2025; Farabi et al., 2024). The performance of an ISSG system is governed by four interrelated material-level requirements: broadband solar light absorption, effective heat confinement at the evaporation interface, continuous capillary-driven water supply, and unimpeded vapor diffusion through the porous scaffold structure. Achieving all four properties simultaneously in a single low-cost material system remains the central challenge in ISSG research (Abdullah et al., 2025).

Two-dimensional MXenes, represented by the general formula $M_{n+1}X_nT_x$ (where M is an early transition metal, X is carbon or nitrogen, and T_x denotes surface functional groups such as –OH, –F, and –O), have emerged as exceptional photothermal candidates owing to their metallic electrical conductivity (up to 10,000 S cm^{-1} for $Ti_3C_2T_x$), near-unity solar absorptance across the UV–NIR spectrum (>90% in the visible–NIR range), high thermal conductivity (up to 200 W m^{-1} K^{-1}), intrinsic hydrophilicity arising from surface hydroxyl and oxygen terminations, and chemical compatibility with aqueous environments (Gogotsi& Huang, 2021; Li *et al.,* 2017a; Liu, 2021; Masekela et al., 2026). $Ti_3C_2T_x$, the most extensively studied MXene, has demonstrated exceptional photothermal conversion efficiencies and has been integrated into a broad range of solar-evaporator architectures (Protyai & Rashid, 2024; Amani *et al.,* 2024). However, conventional $Ti_3C_2T_x$ synthesis routes proceed via selective acid etching of Ti_3AlC_2 MAX phase precursors, which are typically synthesized at 1300–1400°C using pure titanium metal, a costly and energetically intensive starting material. The high synthesis temperature and precursor cost remain significant barriers to the scalable and economically viable production of MXenes for environmental applications (Jolly *et al.,* 2021; Zaed *et al.,* 2024).

Biomass-derived carbon scaffolds have attracted intense interest as sustainable substrates for photothermal evaporators. Among these, luffa sponge, a natural cucurbit, stands out for its three-dimensional (3D) open fibrous network, hierarchical porosity, low thermal conductivity, and intrinsic capillary-driven water transport characteristics (Li et al., 2024; Yao et al., 2022). The thermal carbonization of luffa transforms its native lignocellulosic framework into a macroporous carbon skeleton with enhanced light absorption and thermal stability while preserving the open pore architecture required for continuous water supply and vapor escape (Huang et al., 2023). When combined with a high-

performance photothermal coating, such as $Ti_3C_2T_x$, this substrate offers a synergistic composite in which the carbon scaffold provides structural support, thermal insulation, and capillary transport, while the MXene overlayer delivers broadband solar harvesting and efficient interfacial heat generation (Zhao et al., 2022; Wu et al., 2024).

Despite these complementary strengths, existing studies have largely treated MXene synthesis and the fabrication of MXene-based evaporators as independent research efforts, with no study demonstrating an integrated materials pathway that spans sustainable, low-cost MXene synthesis to the fabrication and rigorous performance validation of a solar desalination device. Specifically, the use of TiO_2 as an alternative titanium source in the molten salt shielding synthesis (MS^3) of the Ti_3AlC_2 MAX phase, which enables an approximately 600°C reduction in the synthesis temperature, and its downstream application in a solar evaporator have not been reported. Closing this gap is essential for establishing a truly sustainable, closed-loop material route for solar water purification.

In this study, we present a comprehensive end-to-end study that addresses this gap. We first demonstrate the MS^3 synthesis of Ti_3AlC_2 MAX phase from cost-effective TiO_2, aluminum, and activated carbon at 1100°C and its conversion to $Ti_3C_2T_x$ MXene through selective HF/HCl etching. MXene was then deployed as a conformal photothermal coating on a carbonized luffa sponge substrate, yielding the MC-CLS composite evaporator. The structural, chemical, optical, and thermal properties of each material at every processing stage were rigorously characterized using SEM, XRD, FTIR, UV–Vis spectroscopy, and TGA. The solar evaporation performance was systematically evaluated across 1–5 kW m^{-2} irradiance, and long-term cycling stability over 21 wetting–drying cycles was demonstrated. Finally, the desalination capability was validated through ICP-OES quantification of the major ions in the condensate against the WHO drinking water standards. The results establish MC-CLS as a high-performance, durable, and sustainable solar desalination platform and validate the MS^3 route as a viable and energy-efficient pathway for MXene production at a reduced cost.

Experimental Section

Materials and Chemicals

Titanium dioxide (anatase, >99% purity), elemental aluminum powder (particle size 44 μm), activated charcoal (particle size 149 μm), sodium chloride (99–100% purity), potassium chloride (>99.5% purity), hydrofluoric acid (HF, 48% purity), hydrochloric acid (HCl, 37%), tetramethylammonium hydroxide (TMAOH, 10 wt% in water), methanol (>99% purity), isopropyl alcohol (IPA), and sodium hydroxide pellets (97% purity) were used for MAX phase and MXene synthesis. Pristine luffa sponge was sourced from Firo, Bauchi State, Nigeria. Deionized (DI) water was used throughout. For simulated seawater preparation, sodium chloride (NaCl, ≥99%), sodium bicarbonate ($NaHCO_3$, ≥99%), sodium sulfate (Na_2SO_4, ≥99%), potassium chloride (KCl, ≥99%), magnesium chloride ($MgCl_2$, ≥99%), magnesium sulfate ($MgSO_4$, ≥99%), and calcium chloride ($CaCl_2$, ≥99%) were supplied by J&K Scientific Ltd. (Beijing, China). All reagents were used as received without further purification.

Molten-Salt-Shielded Synthesis of Ti_3AlC_2 MAX Phase

Ti_3AlC_2 was synthesized via a modified MS^3 route adapted from Yang *et al.,* (2019), using TiO_2 and activated carbon as substitutes for pure titanium metal and acetylene black, respectively. Precursor powders of TiO_2, Al, and activated carbon were weighed at a molar ratio of TiO_2 :Al:C = 3:1:2, corresponding to 2.002 g TiO_2, 0.230 g Al, and 0.200 g C. The mixture was subjected to planetary ball milling in methanol (ball-to-powder ratio 15:1) for 12 h. Following gentle drying at ~45°C, the dried powder was blended with a eutectic NaCl–KCl (1:1 molar) salt mixture using a mortar and pestle at a salt-to-sample weight ratio of 7:3. The blended mixture was transferred to an alumina crucible inside a horizontal tube furnace, purged with high-purity Ar (99.999%) at 40 mL min^{-1}, and heated to 1100°C at 5°C min^{-1}, held for 2 h, then allowed to cool naturally. The solidified product was washed by ultrasonication in DI water at 80°C until the electrical conductivity of the filtrate approached that of pure DI water, vacuum-filtered, dried at 80°C for 12 h, and stored in sealed glass vials.

Selective Etching to $Ti_3C_2T_x$ MXene

Multilayer $Ti_3C_2T_x$ was synthesized via an HF/HCl wet etching protocol following Shuck *et al.* (2020). All procedures involving HF were conducted using HF-resistant

polypropylene vessels under rigorous personal protective equipment protocols. Briefly, 12 mL HCl was added to 6 mL DI water; 2 mL HF was introduced dropwise with continuous stirring. Ti_3AlC_2 powder (0.5 g) was added gradually over 4–5 min to control the exothermic reaction. The suspension was stirred at 35°C for 24 h in a closed (gas-venting) vessel. The product was isolated by repeated centrifugation (4000 rpm, 5 min per cycle) and DI water washing until the supernatant reached neutral pH, as monitored by litmus paper. The sediment was resuspended in TMAOH solution and stirred for 12 h to facilitate delamination, then washed to neutral pH, vacuum-filtered, and dried at 120°C for 3 h under vacuum. The resulting solid $Ti_3C_2T_x$ MXene was stored in air-tight glass vials to prevent oxidation.

Preparation of the Carbonized Luffa Sponge Substrate

Cylindrical luffa sponge sections were bisected longitudinally and the central vascular bundle removed with surgical scissors. Discs of 40 mm diameter and 12 mm thickness were ultrasonicated three times in DI water and three times in absolute ethanol (10 min per cycle), then oven-dried at 55°C to constant mass. Carbonization was performed by placing dried luffa discs on a preheated hot plate at 500°C for 30 s in ambient atmosphere (Liu et al., 2020) , converting the outer fibrous network into a broadband light-absorbing carbon framework while preserving the macroporous scaffold architecture. The resulting carbonized luffa sponge (CLS) was uniformly black; disintegrated fibers were removed and specimens stored in a desiccator.

Fabrication of the MC-CLS Photothermal Composite

$Ti_3C_2T_x$ MXene was deposited onto CLS substrates by a controlled dip-coating protocol. A stable MXene suspension at 3 mg mL^{-1} in DI water was prepared by bath ultrasonication (30 min) followed by gravitational settling to remove coarse aggregates. CLS discs were fully immersed in the suspension for a dwell time of 1–5 min, then slowly withdrawn to deposit a conformal coating. After each dip-and-withdraw cycle, the specimen was dried at 40–60°C for 10–20 min on a hot plate. This dip-coating cycle was repeated 3–8 times with freshly agitated suspension per cycle to incrementally build the MXene overlayer. The final specimen was oven-dried at 60°C for ≥2 h and optionally annealed at 100–150°C for 30 min to enhance interfacial adhesion. The thickness of the absorber disc was systematically varied (6, 10, 12, 14, and 16 mm) to optimize solar-to-steam efficiency, as

described in Section 3.4. All subsequent performance characterization was conducted on the 12 mm optimum specimen.

Characterization

Scanning electron microscopy and energy-dispersive X-ray spectroscopy (SEM-EDX) were performed using a Hitachi S4800 (Japan) for MC-CLS and a Phenom ProX system for MAX/MXene specimens, each sputter-coated with 5 nm Au before imaging. X-ray diffraction (XRD) was conducted using a PANalytical X'Pert PRO diffractometer (Cu-Kα radiation, λ = 1.5406 Å, 40 kV, 25 mA) over 2θ = 0–80° at 120 min^{-1}. FTIR spectra were recorded in attenuated total reflectance (ATR) mode over 400–4000 cm^{-1} on a Bruker VERTEX 70 instrument (for MC-CLS) and a Bruker Alpha II (for MAX/MXene). UV–Visible spectra were acquired using an Agilent Cary 5000 (200–1100 nm, diffuse reflectance for MC-CLS) and a LAMBDA 750 Perkin Elmer spectrophotometer (for MXene suspensions at 0.03 mg mL^{-1} in DI water, quartz cuvette, 200–1500 nm). Thermogravimetric analysis (TGA) was performed using a Hot Disk TPS 2500s instrument under N_2 atmosphere (10°C min^{-1}, 25–500°C). Surface temperatures during solar evaporation were monitored using an infrared thermal camera (HT-18).

Solar Evaporation Testing

Interfacial solar evaporation experiments were conducted under AM 1.5G simulated illumination (300 W xenon lamp, PLS-SXE300, Beijing Perfect Light Technology, China) at laboratory conditions of 23–25°C and 40–50% relative humidity as shown in fig. 1. Irradiance at the sample plane (1–5 kW m^{-2}) was calibrated with a Thorlabs S314C optical power meter. The MC-CLS (40 mm diameter) was floated at the water–air interface of a water reservoir and equilibrated in the dark for 10 min to ensure complete capillary priming. Mass loss was recorded at 10 s intervals for 60 min using a computer-interfaced Ohaus CP213 analytical balance (±0.1 mg). All experiments were performed in quadruplicate (n = 4). Control runs comprised pure water, pristine LS without MXene, and dark-evaporation baselines. Evaporation rate v (kg m^{-2} h^{-1}) and solar-to-steam conversion efficiency η were calculated according to Equations (1) and (2) (Wu et al., 2023):

$$V = \frac{\Delta m}{\Delta t . A} \quad (1)$$

$$\eta = \frac{\dot{m}(h^{L\beta} + C\Delta T)}{(I \cdot A)} \quad (2)$$

where Δm is the net evaporated mass (kg), A is the projected absorber area (m^2), Δt is the measurement interval (h), $\dot{m} = \Delta m/\Delta t$ (kg s^{-1}), $h^{L\beta} \approx 2.26 \times 10^6$ J kg^{-1} is the latent heat of vaporization at 25°C, CΔT is the sensible heat contribution, and I (W m^{-2}) is the incident solar irradiance.

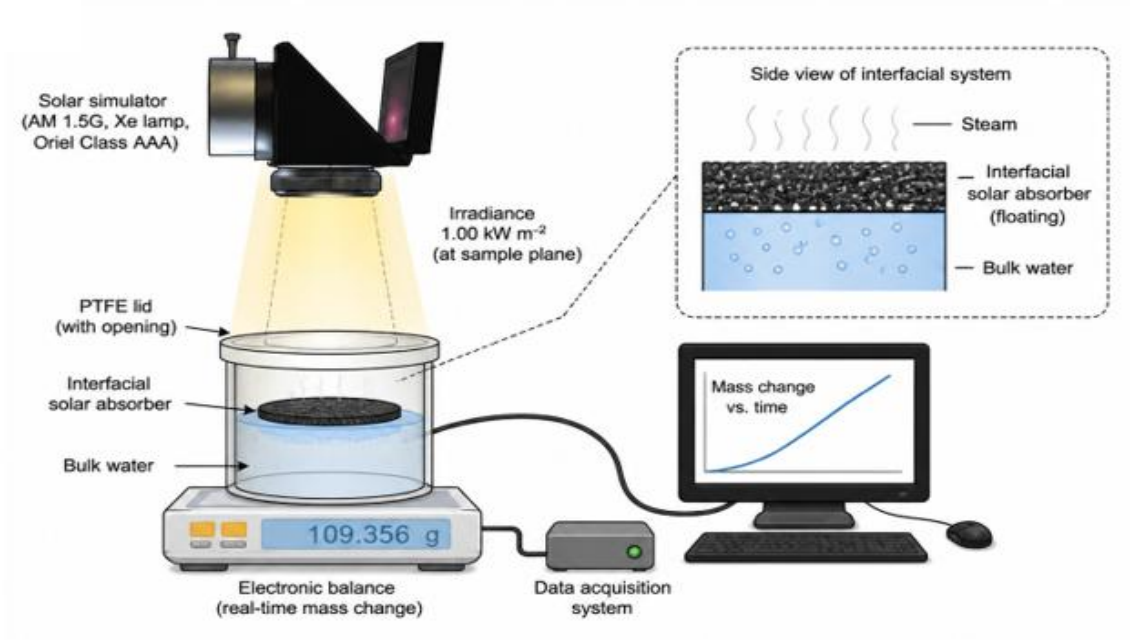


Figure 1. Schematic diagram of the laboratory setup for solar evaporation evaluation

Desalination Performance Assessment

Simulated seawater was prepared by dissolving 6.68 g NaCl, 0.05 g $NaHCO_3$, 0.87 g Na_2SO_4, 0.18 g KCl, 0.57 g $MgCl_2$, 0.81 g $MgSO_4$, and 0.28 g $CaCl_2$ in 250 mL DI water (Ma et al., 2017). NaCl solutions of 0.1, 1, 10, 20, and 25 wt% were prepared to span brackish to hypersaline feed conditions. Solar evaporation was conducted as described above, and vapor was condensed using a cold-finger condenser. Condensate cation concentrations (Na^+, K^+, Ca^{2+}, Mg^{2+}) were quantified by inductively coupled plasma optical emission spectrometry (ICP-OES) and benchmarked against WHO Guidelines for Drinking-Water Quality. All measurements were performed in quadruplicate.

Results and Discussion

Characterization of Ti_3AlC_2 MAX Phase

Morphological Analysis (SEM)

The SEM micrographs of the MS[3]-synthesized Ti_3AlC_2 (Fig. 2a) reveal a dense and compact morphology with well-defined stacked layers, characteristic of a successfully synthesized Ti_3AlC_2 MAX phase structure (Rasool *et al.,* 2019; Alhabeb *et al.,* 2017). The aligned lamellar architecture, analogous to natural flake graphite, confirms that the selected synthesis temperature (1100°C) and heating rate (5°C min^{-1}) were appropriate for the solid-state reaction between TiO_2, Al, and activated carbon in the molten salt medium. Each layer was uniform in shape and size, indicating homogeneous nucleation and growth facilitated by the NaCl–KCl flux. The dense, compact structure is critical because it provides a well-ordered lamellar template for the subsequent selective etching step, where the accessibility of Al-containing interlayers to the etchant directly determines the MXene yield and quality. Minor secondary phases, consistent with residual TiC or Al_2O_3, which are commonly observed in MAX phase synthesis from TiO_2-based precursors (Yang *et al.,* 2019; Liu *et al.,* 2020; Jolly *et al.,* 2021), are expected to be eliminated during selective etching.

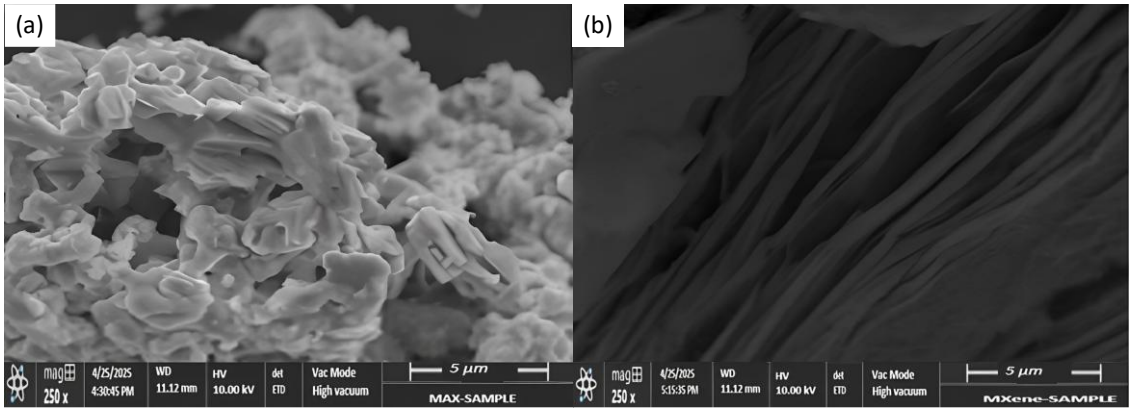


Figure 2. SEM Images (a) Ti_3AlC_2 MAX Phase (b) $Ti_3C_2T_x$ MXene

Crystallographic Analysis (XRD)

The XRD pattern of the synthesized Ti_3AlC_2 (Fig. 3a) displays characteristic diffraction peaks at 2θ ≈ 9°, 18°, 31°, 41°, and 68°, which are assigned to the (002), (004), (101), (104), and (107) planes of the hexagonal Ti_3AlC_2 MAX phase structure (JCPDS 52-0875), respectively. The sharp and well-resolved peaks confirmed the high degree of crystallinity. The strong (002) and (004) reflections at low 2θ values are consistent with a

well-ordered nanolaminated architecture with a c-lattice parameter characteristic of Ti_3AlC_2 stoichiometry. Minor peaks attributable to TiC or Al_2O_3 secondary phases were observed, as is typical for MAX phase synthesis from oxide precursors (Yang *et al.,* 2019; Liu *et al.,* 2020), and are associated with the partial reduction of TiO_2 by activated carbon under the synthesis conditions. Notably, the successful synthesis of Ti_3AlC_2 at 1100°C, well below the conventional 1300–1400°C required for solid-state routes using pure Ti, validates the energy-reducing effect of the molten NaCl–KCl flux, which enhances mass transport and reaction kinetics through liquid-phase diffusion pathways (Dash *et al.,* 2019).

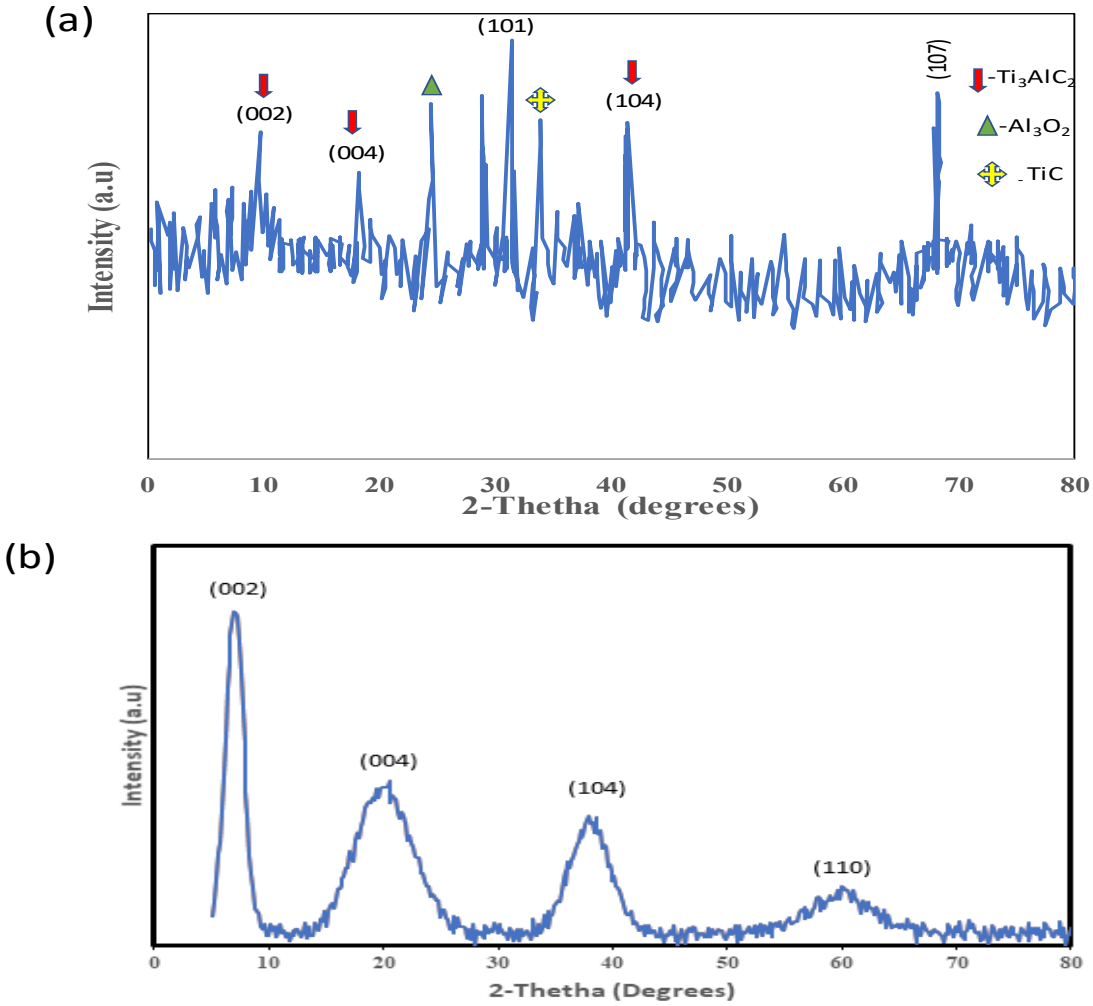


Figure 3. XRD of (a) Ti_3AlC_2 MAX Phase; (b) Ti_3C_2Tx MXene

Surface Chemistry (FTIR)

The FTIR spectrum of Ti_3AlC_2 (Fig. 4) exhibits characteristic absorption bands near 500 cm^{-1} and 670 cm^{-1}, corresponding to Al–C and Ti–C bond stretching vibrations,

respectively, which are the definitive spectroscopic signatures of an intact Ti_3AlC_2 MAX phase framework (Parker et al., 2024). The presence of these well-resolved metallic carbide bands confirms that the reactive sintering of TiO_2, Al, and activated C was achieved successfully under MS^3 conditions. No significant O–H or C–O bands are observed, consistent with the removal of surface oxides and organic solvents during washing and drying.

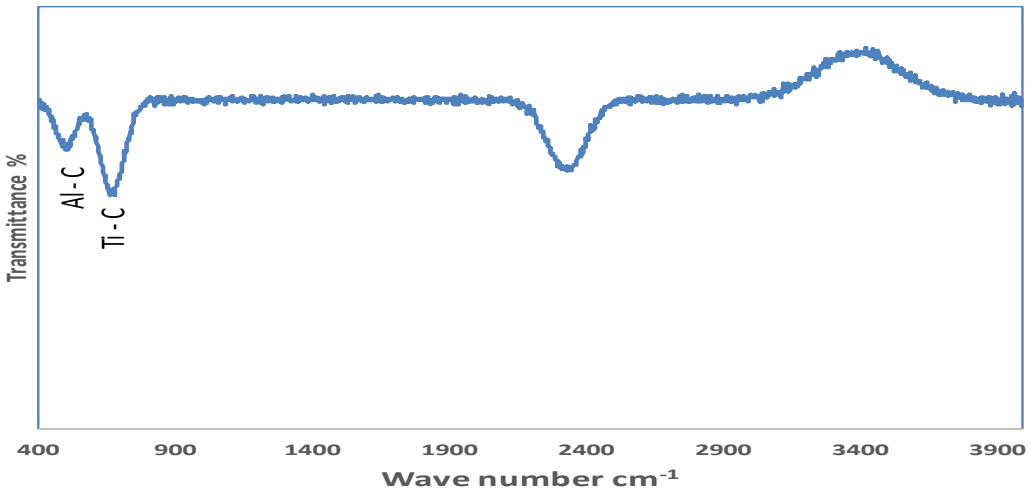


Figure 4. FTIR of Ti_3AlC_2 MAX Phase

Characterization of $Ti_3C_2T_x$ MXene

Morphological Transformation (SEM)

In stark contrast to the dense compact morphology of the MAX phase precursor (Fig. 2a), the SEM image of $Ti_3C_2T_x$ MXene (Fig. 2b) reveals a characteristic accordion-like expanded sheet structure with clearly separated, few-layer nanolaminate morphology. This structural transformation is the most visually compelling evidence of successful aluminum etching and MXene delamination. The increased interlayer separation and reduced layer compactness arise from the removal of Al layers by HF, the simultaneous intercalation of water molecules and TMAOH between the $Ti_3C_2T_x$ layers, and the development of surface functional groups (T_x = –OH, –F, –O) that introduce steric and electrostatic repulsion between adjacent sheets (Gogotsi & Anasori, 2019). The accordion morphology provides a high specific surface area with abundant accessible active sites for photothermal absorption and surface-enhanced heat transfer, making it ideal for coating applications.

Structural Evolution (XRD)

The XRD pattern of the synthesized $Ti_3C_2T_x$ (Fig. 3b) shows a dominant (002) peak shifted to $2\theta \approx 7°$ from approximately 9° in the MAX phase precursor, accompanied by significant broadening and reduction in peak intensity. This low-angle shift directly corresponds to an increase in the c-lattice parameter (d-spacing), reflecting the expansion of the interlayer spacing consequent upon Al removal and the intercalation of water and functional groups between the $Ti_3C_2T_x$ layers (Ghidiu *et al.* 2014). Additional broad reflections at approximately 19°, 39°, and 60° are consistent with the (004), (104), and (110) planes characteristic of the $Ti_3C_2T_x$ structure (Shekhirev *et al.,* 2021). The disappearance of the higher-order MAX phase reflections (101), (104), and (107) confirms the complete transformation from the 3D MAX architecture to the 2D MXene structure. The maintained presence of the (002) reflection, despite its broadening, confirms the retention of the layered, two-dimensional structural order essential for the photothermal and electronic properties of MXene.

Functional Group Analysis (FTIR)

A comparison of the FTIR spectra of Ti_3AlC_2 (Fig. 4) and $Ti_3C_2T_x$ (Fig. 5) provides definitive chemical evidence for the MAX-to-MXene transformation. In the MXene spectrum, the Al–C absorption band previously present at ~500 cm^{-1} in the MAX phase is completely absent, confirming the successful and near-complete removal of the aluminum interlayers (Halim *et al.* 2014). New vibrational features emerged in the MXene spectrum: Ti–C stretching at 670 cm^{-1}, Ti–F bending at 731 cm^{-1}, C–F stretching at 1117 cm^{-1}, C–H bending at 1404 cm^{-1}, C–O stretching at 1615 cm^{-1}, and a broad O–H stretching band at 3368 cm^{-1}. The broad O–H band confirms the introduction of hydroxyl surface terminations during the acid etching process, which are critical for both the colloidal stability of the MXene suspension and the capillary-compatible wetting behavior required in solar evaporation applications. All assignments were consistent with the reference FTIR spectral library for $Ti_3C_2T_x$ MXene (Parker et al., 2024).

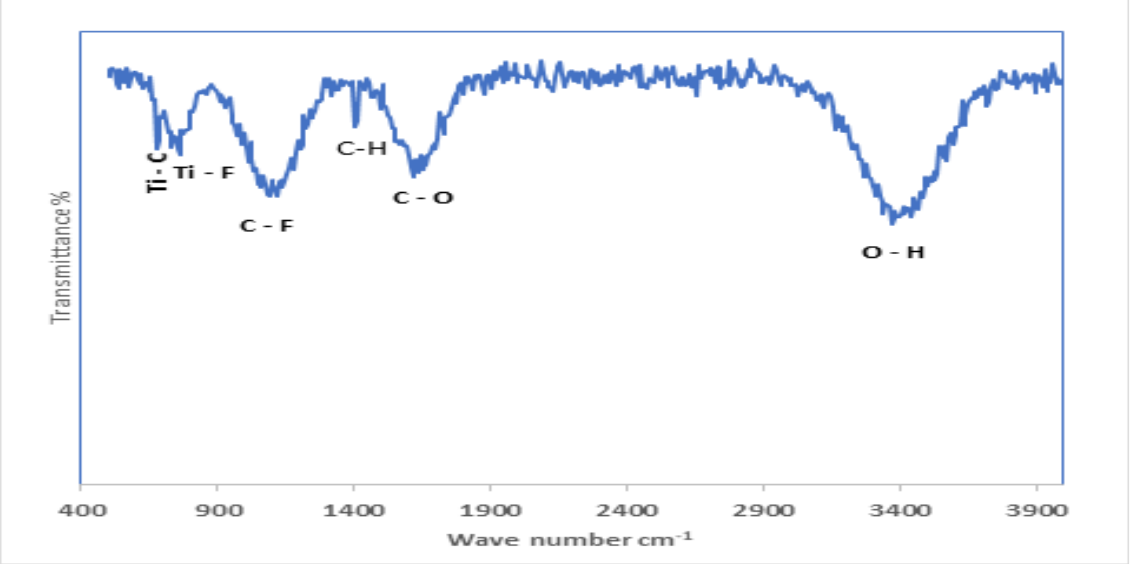


Figure 5. FTIR of Ti_3C_2Tx MXene

Optical Properties (UV–Vis Spectroscopy)

The UV–Vis absorption spectrum of the $Ti_3C_2T_x$ MXene suspension (Fig. 6) exhibits two characteristic features: a distinct peak at approximately 263 nm and a broad absorption band centered near 792 nm. The peak at ~263 nm is attributed to $\pi \rightarrow \pi^*$ transitions in sp^2-hybridized carbon domains, consistent with the incorporation of activated carbon-derived graphitic or disordered carbon structures within or on the surface of the MXene product (Bu *et al.* 2020). This finding is significant because it confirms that the use of activated carbon as the carbon precursor in the MS^3 synthesis introduces electronically conductive carbon-rich phases that may synergistically enhance the photothermal performance of the final material. The more prominent broad absorption feature at ~792 nm aligns with the localized surface plasmon resonance (LSPR) and interband transitions characteristic of $Ti_3C_2T_x$ MXene, arising from the collective oscillations of delocalized conduction electrons in the two-dimensional metallic lattice (Dillon *et al.,* 2016; Hao *et al.,* 2022). The observation of this plasmonic absorption in the NIR region is of particular relevance for solar desalination, where NIR photons constitute approximately 50% of the terrestrial solar spectrum. The spectral profile matches the reported UV–Vis characteristics of $Ti_3C_2T_x$ synthesized by selective etching of Ti_3AlC_2 from conventional precursors (Soman *et al.,* 2024), validating the optical quality of the MXene produced from the alternative TiO_2-based MS3 route.

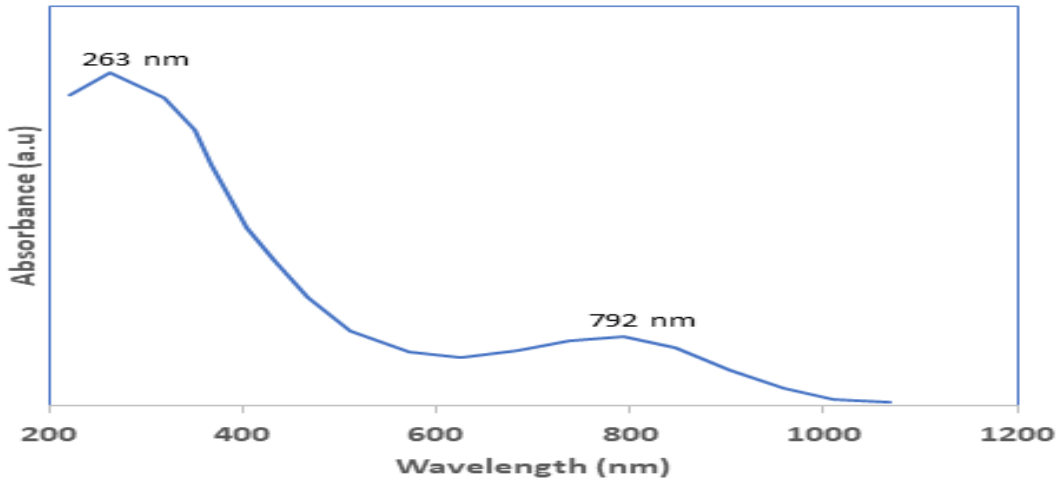


Figure 6. UV-VIS Absorption spectra of $Ti_3C_2T_x$ MXene

Characterization of the MC-CLS Photothermal Composite

Morphology and Elemental Composition (SEM-EDX)

SEM micrographs of the pristine luffa sponge (Fig. 7a–b) reveal a characteristic open-pore, fiber-shaped network with individual fiber surfaces that are relatively smooth. After thermal carbonization and $Ti_3C_2T_x$ dip-coating, the fiber surfaces of MC-CLS (Fig. 7c) are uniformly enveloped by $Ti_3C_2T_x$ nanosheets, rendering them appreciably rougher than the uncoated CLS substrate. This increased surface roughness is expected to promote multiple internal light scattering within the porous architecture, reducing specular reflectance and enhancing broadband solar absorptance through photon recycling. The spatial selectivity and conformity of the dip-coating process are clearly evident at the boundary between coated and uncoated regions in reference specimens. EDX analysis of MC-CLS (Fig. 7d) confirms the presence of titanium, carbon, and oxygen at compositions consistent with the $Ti_3C_2T_x$ stoichiometry, providing direct elemental evidence of successful MXene deposition across the carbonized fiber network.

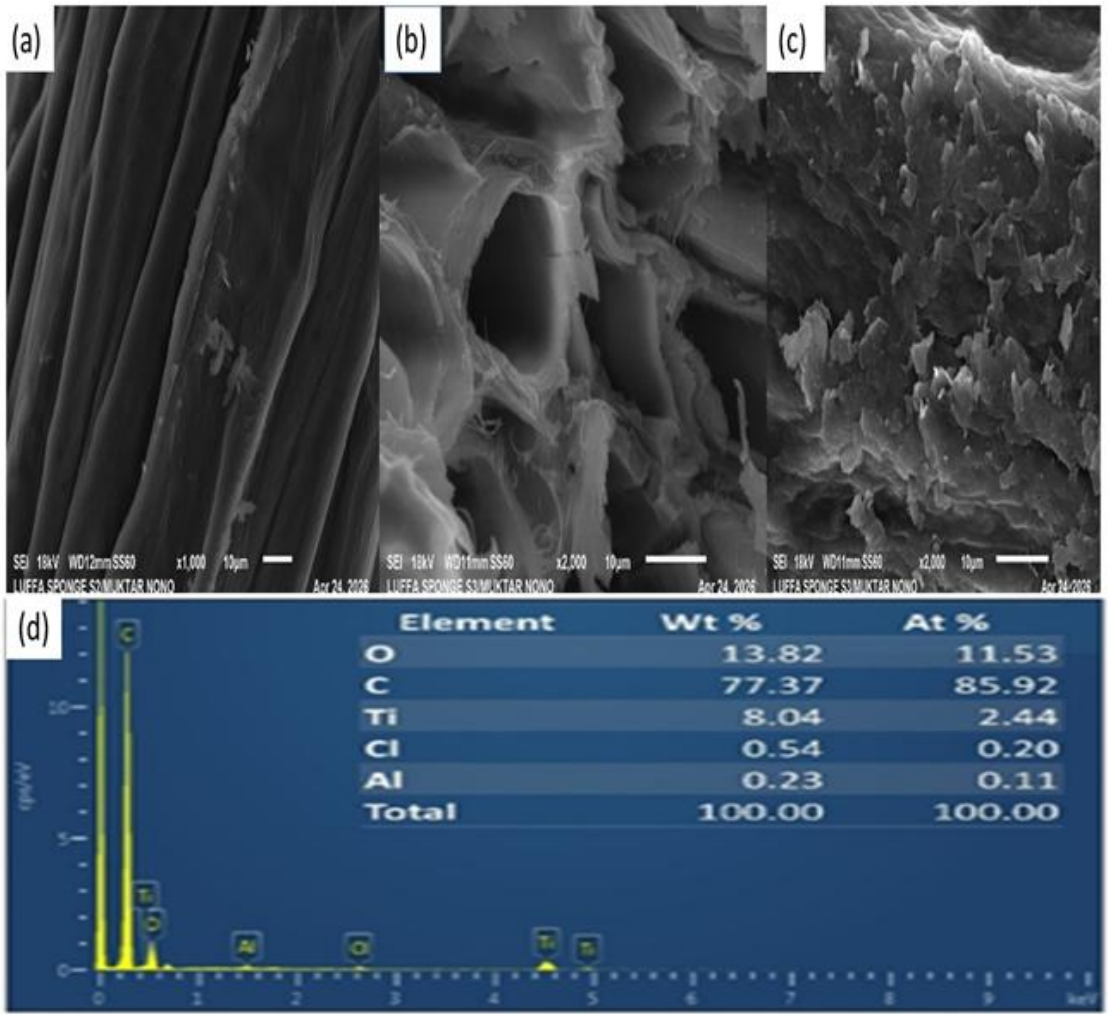


Figure 7. SEM micrographs of (a) pristine luffa sponge (LS), (b) cross-section of LS, (c) MXene-coated carbonized luffa sponge (MC-CLS), and (d) EDX spectrum and elemental mapping of MC-CLS.

Chemical Integration (FTIR)

The FTIR spectrum of pristine luffa sponge displays the hallmark absorption bands of a native lignocellulosic biopolymer: a broad O–H stretching envelope at 3200–3500 cm^{-1} from hydroxyl groups in cellulose and hemicellulose, aliphatic C–H stretching near 2900 cm^{-1}, carbonyl C=O stretching at ~1740 cm^{-1} (hemicellulose esters), and C–O–C glycosidic linkages at 1050–1150 cm^{-1} (Figure 8a). After carbonization and MXene coating, the MC-CLS spectrum exhibits several diagnostic modifications. The O–H absorption band is substantially attenuated, consistent with thermal dehydration and partial polysaccharide decomposition at 500°C. New features emerge at 500–800 cm^{-1}, attributed to Ti–C and Ti–O stretching of the MXene lattice, and near 1060–1100 cm^{-1}, associated with Ti–OH surface

terminations. The persistence of hydrophilic Ti–OH terminations in the MC-CLS composite is particularly important because these groups sustain capillary-driven water transport through the MXene-coated fiber network during solar evaporation, ensuring continuous liquid supply to the evaporation front.

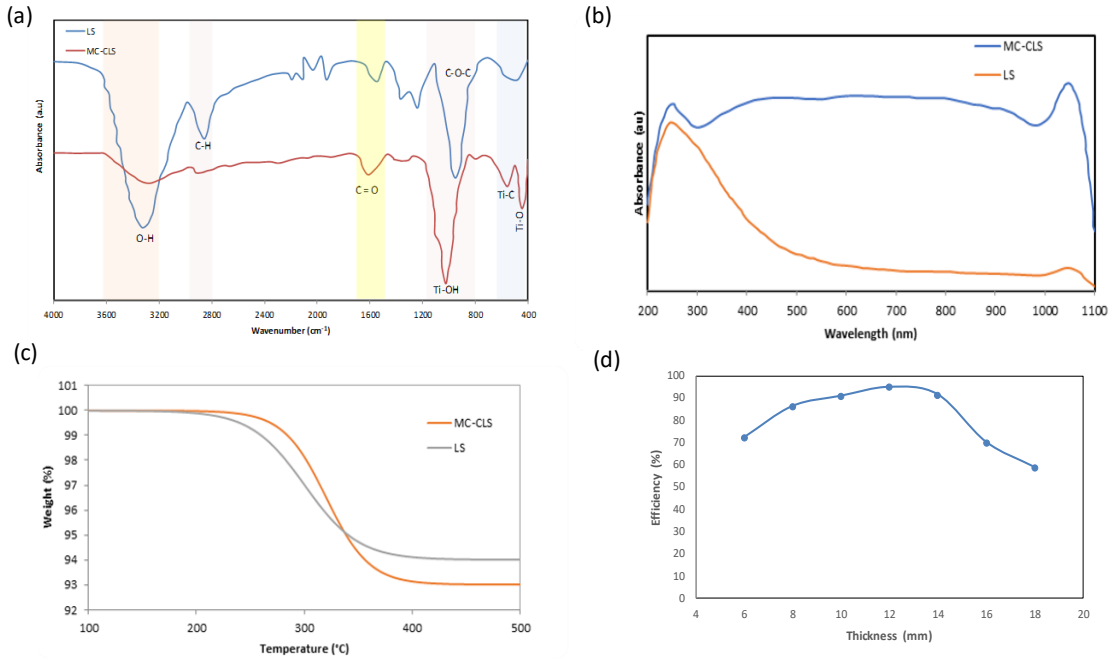


Figure 8. (a) FTIR Spectra of LS & MC-CLS; (b) UV-Visible Spectra of LS & MC-LS; (c) TGA curves of LS and MC-CLS and (d) Evaporation efficiency at different thickness

Broadband Solar Absorptance (UV–Vis)

The UV–Vis diffuse reflectance spectra over 200–1100 nm (Fig. 8b) illustrates the dramatic optical contrast between pristine luffa sponge and MC-CLS. The pristine LS exhibits near-zero absorptance throughout the measured spectral range, reflecting its predominantly transparent lignocellulosic composition that lacks π-conjugated systems and free charge carriers required for efficient photon absorption. In stark contrast, MC-CLS demonstrates strong, broadband absorption across the entire spectral region with no distinct peaks but a consistently elevated, essentially flat absorptance profile (≥0.95). This behavior is characteristic of highly conductive, carbon-rich composite materials in which the π-electron systems of the carbonized scaffold and the metallic conductivity of $Ti_3C_2T_x$ synergistically facilitate efficient photon capture and rapid non-radiative dissipation as heat. The near-unity solar absorptance of MC-CLS across the UV, visible, and NIR spectral regions, combined

with its thermal insulation capacity and capillary water transport, satisfies all four key performance criteria of an efficient ISSG evaporator.

Thermal Stability (TGA)

TGA analysis under N_2 atmosphere (Fig. 8c) reveals markedly different decomposition profiles for LS and MC-CLS. Pristine LS undergoes three kinetically distinct decomposition stages: Stage I (ambient to ~100°C, ~6–8 wt% loss) from desorption of physically adsorbed and bound moisture; Stage II (250–370°C, ~55–65 wt% loss) from concurrent depolymerization of hemicellulose (onset ~220°C) and cellulose (onset ~315°C); and Stage III (370–500°C, ~10–15 wt% loss) from thermal degradation of the heterogeneous lignin network. The residual mass of pristine LS at 500°C is <10 wt%, confirming near-complete volatilization of the organic lignocellulosic constituents. The MC-CLS TGA profile is fundamentally distinct: the major hemicellulose/cellulose decomposition event is entirely absent, confirming that carbonization at 500°C has already converted the thermally labile polysaccharide constituents into a stable graphitic carbon framework. The modest mass loss below 100°C (~3–6%) reflects residual moisture adsorbed on the hydrophilic Ti–OH MXene terminations, while the total mass loss within the solar evaporation operating range (ambient to ≤100°C) does not exceed ~6%, confirming complete thermochemical stability under operational conditions. The substantially higher residual mass of MC-CLS at 500°C (>60 wt%) provides a semi-quantitative measure of the total $Ti_3C_2T_x$ and graphitic carbon content of the composite.

Optimization of Absorber Thickness

The thickness of the MC-CLS absorber disc governs two competing physical processes that collectively determine the solar-to-steam conversion efficiency: thermal confinement at the evaporation interface and capillary-driven water transport from the bulk reservoir to the absorber surface. A systematic study of absorber thickness (6, 10, 12, 14, and 16 mm) was conducted under 1 kW m^{-2} illumination. The efficiency displayed a non-monotonic dependence on thickness with a well-defined maximum at 12 mm (Fig. 8d). Efficiency increased progressively from 72.16% at 6 mm to 90.92% at 10 mm, reaching its peak value of 94.97% at 12 mm, before declining to 91.62% at 14 mm and 70.15% at 16 mm.

The ascending branch (6–12 mm) is governed by the thermal insulation function of the absorber. Thinner specimens provide inadequate thermal resistance between the illuminated top surface and the cooler bulk water below, resulting in a significant fraction of the photothermal energy being conducted downward into the bulk reservoir rather than driving evaporation. As the thickness increases from 6 to 12 mm, the thermal resistance of the porous carbon–MXene scaffold increases proportionally, reducing conductive losses to the bulk and increasing the fraction of absorbed solar energy directed into the latent heat of evaporation. This behavior is consistent with the heat confinement model described by (Gao et al., 2018) for interfacial evaporator optimization.

The descending branch (12–16 mm) reflects the increasing dominance of capillary water transport resistance. As thickness increases beyond 12 mm, the capillary path length traversed by water from the wetted underside to the evaporation front increases proportionally, raising the viscous resistance according to Darcy's law (Chebbi, 2021). At the 12 mm optimum, the capillary driving force is precisely sufficient to maintain uninterrupted liquid supply under the maximum evaporation flux at 1 sun, while greater thicknesses introduce transport limitations that create localized dry-out events at the evaporation front, reducing effective evaporation area and overall efficiency. The 12 mm thickness represents the thermodynamic optimum at which the competing requirements of heat confinement and water supply are simultaneously and optimally satisfied. This thickness was adopted for all subsequent performance measurements.

Solar Evaporation Performance

Baseline and Comparative Performance

The evaporation performance and solar-thermal conversion efficiency of the three samples under 1 sun irradiation and in the dark are compared in Figure 9. Pure water, serving as the baseline, exhibits the lowest solar-driven evaporation rate of 0.34 kg m^{-2} h^{-1} with a corresponding solar-thermal conversion efficiency of only 14.8%. This poor performance is expected given that bulk water absorbs solar energy inefficiently and lacks any localized heat management, resulting in significant thermal losses to the surrounding environment. Pristine LS demonstrates a substantially improved evaporation rate of 1.30 kg m^{-2} h^{-1} under irradiation, nearly four times that of pure water, along with an efficiency of 57.0%. This improvement is attributed to the inherent porous and hydrophilic architecture

of the loofah, which facilitates rapid capillary-driven water transport to the evaporation surface and provides a degree of thermal localization that reduces heat dissipation into the bulk water. The MC-CLS evaporator achieves the highest performance among the three samples, reaching an evaporation rate of 2.11 kg m^{-2} h^{-1} and a solar-thermal conversion efficiency of 94.0%. This remarkable enhancement over both pure water and the pristine loofah sponge reflects the synergistic contribution of the carbonization and MXene coating deposited onto the loofah framework. Under 1 sun irradiation, the surface temperature of MC-CLS reaches 36.2 °C after 60 min, which is higher than that of pristine loofah (29.5 °C), attributed to improved light absorption induced by carbonization and MXene coating. The surface temperature increases progressively to 45 °C, 56 °C, 67 °C, and 78 °C under 2, 3, 4, and 5 sun irradiances, respectively.

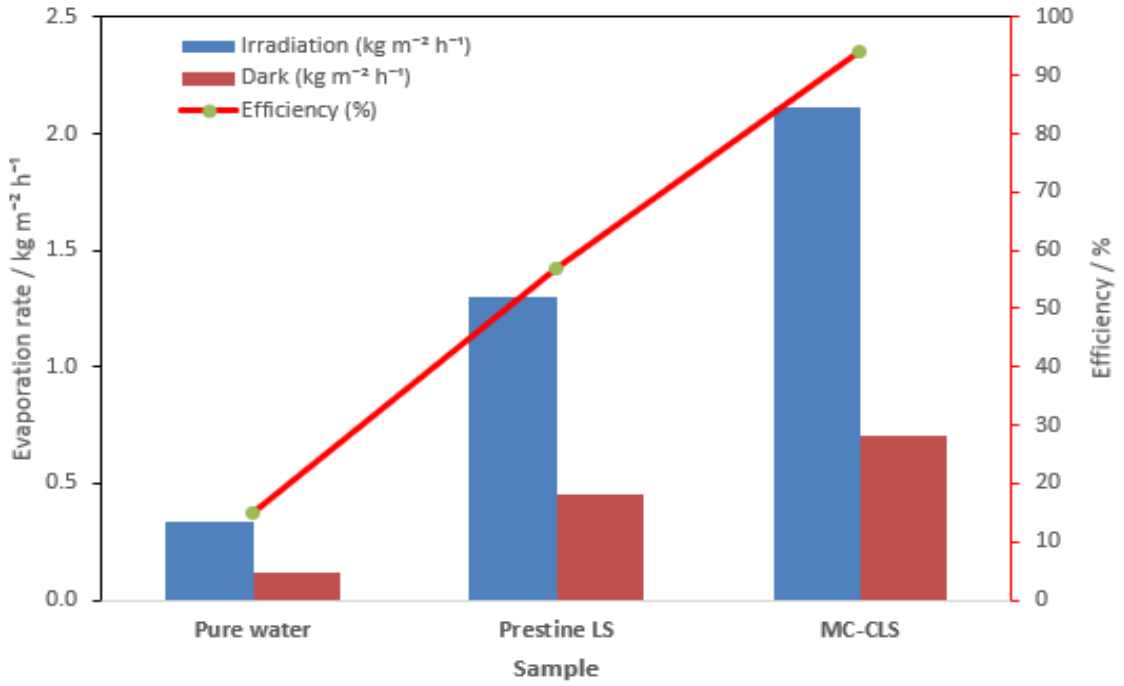


Figure 9. Comparison of solar steam generation rates of pure water, loofah, HL, HLM, and HLMC evaporators under 1 sun irradiation and in the dark and corresponding energy efficiencies

Enhanced Evaporation Rate and Conversion Efficiency of MC-CLS

The integration of $Ti_3C_2T_x$ MXene onto the carbonized luffa sponge dramatically enhanced solar evaporation performance. Under one-sun illumination, MC-CLS achieved an average evaporation rate of 2.12 kg m^{-2} h^{-1} (calculated using mass loss information on figure 10a), representing a 6.00-fold enhancement relative to DI water and a 1.6-fold enhancement

relative to pristine luffa. The solar-to-steam conversion efficiency was 94%, a 6.5-fold improvement over the bare water reference of 14.8%. The superb water evaporation performance of MC-CLS is attributed to the following factors: its black appearance resulting during the carbonization which enhances solar light absorption. The photothermal effects of MXene and the thermal vibration of amorphous carbon augment solar−thermal energy harvesting. The hydrophilicity of MC-CLS facilitates the upward transport of water to the evaporation surface. These efficiency values are competitive with leading MXene-based photothermal evaporators reported in the literature (Table 1), particularly given the entirely low-cost, sustainable synthesis route employed for the MXene component.

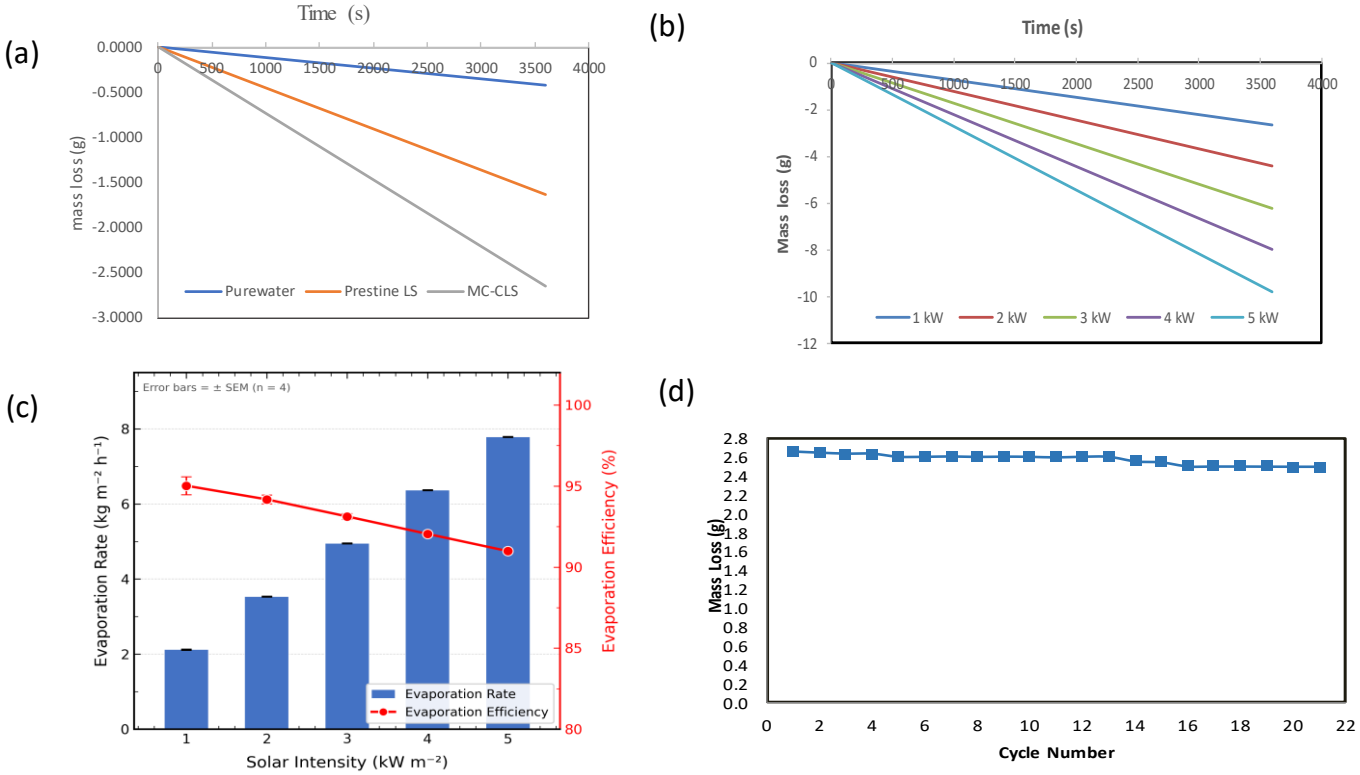


Figure 10. The solar evaporation mass loss of water over time (a) with different absorbers under one sun illumination; (b) with MC-CLS under various solar irradiance; (c) corresponding evaporation rate (star) and the evaporation efficiency (square) under various solar irradiance; (d) mass loss using MC-CLS for 21 cycles (each cycle corresponds to 1 h under 1 kW m^{-2} irradiance)

Table 1. Comparative Solar Evaporation Performance of Selected MXene-Based Photothermal Evaporators at 1 kW m^{-2}

Photothermal Material	Substrate	Evap. Rate (kg m^{-2} h^{-1})	Efficiency (%)	Reference
$Ti_3C_2T_x$ MXene	Kapok fiber	1.47	90.4	(Chen et al., 2022)
$Ti_3C_2T_x$ MXene	Cellulose Acetate	1.33	—	(K. Li et al., 2019)
$Ti_3C_2T_x$ MXene	PVA hydrogel	2.71	90.7	(Yu & Wu, 2020)
$Ti_3C_2T_x$ / CNT	Cotton fabric	1.35	—	(Wang et al., 2021)
MXene/g-C_3N_4	Natural latex foam	1.85	93.5	(Ginting et al., 2022)
Janus VA-MXA	PTFE mold	1.46	>87	(Zhang et al., 2019)
$Ti_3C_2T_x$	Carbonized luffa sponge	2.12	95	This work

Irradiance-Dependent Performance (1–5 kW m^{-2})

Time-resolved mass loss profiles at each irradiance level (Fig. 10b) exhibited excellent linearity throughout the 3600 s measurement window, confirming steady-state evaporation without onset of surface dry-out, salt-induced pore blocking, or structural degradation at elevated flux densities. The calculated steady-state evaporation rate increased from 2.12 kg m^{-2} h^{-1} at 1 kW m^{-2} to 7.79 kg m^{-2} h^{-1} at 5 kW m^{-2}, exhibiting a near-linear relationship. This proportional scaling is thermodynamically expected in the regime where solar absorptance and thermal insulation are irradiance-independent: an n-fold increase in photon flux generates an n-fold increase in photothermal heat production and evaporation flux (Wilson et al., 2025). The solar-to-steam conversion efficiency at 1 kW m^{-2} was 95%. At 2, 3, 4- and 5-kW m^{-2}, the efficiency undergoes a moderate decline due to the amplified heat loss pathways described above; however, the total efficiency variation across the entire 1–5 kW m^{-2} range is remarkably small, confirming the 'irradiance-robustness' of MC-CLS (Fig. 10c). This property has substantial practical significance because a device maintaining high conversion efficiency across a five-fold range of solar intensities will deliver proportionally higher annual water output in real-world deployment where solar irradiance varies diurnally and seasonally (Shafaee & Goharshadi, 2025).

Long-Term Cycling Stability

Durability under repeated operational cycling is a critical prerequisite for solar desalination. MC-CLS was evaluated over 21 consecutive wetting–drying cycles, each comprising a one-hour solar evaporation experiment under 1 kW m^{-2}, followed by oven drying at 55°C for one hour (Fig. 10d). After 21 complete cycles, MC-CLS retained >1.98 kg m^{-2} h^{-1}, representing at least 94% of its initial performance level. This exceptional cycling durability can be attributed to three synergistic structural mechanisms. First, the multi-modal attachment of $Ti_3C_2T_x$ nanosheets to the carbonized fiber surface through electrostatic attraction, van der Waals forces, and coordinative hydrogen bonding between MXene Ti and OH terminations and residual oxygen-containing functional groups on the carbon matrix provides robust anchoring that resists hydrodynamic desorption during rapid wetting. Second, the carbon matrix functions as an oxidation barrier, physically shielding MXene nanosheet surfaces from dissolved oxygen and UV-generated reactive oxygen species in the pore water, thereby inhibiting the progressive oxidation of $Ti_3C_2T_x$ to photothermally inactive TiO_2, which is the primary cause of the performance decline in unprotected MXene photothermal devices (Thomas et al., 2025). Third, the hierarchical macropore architecture of the luffa scaffold accommodates the volumetric expansion and contraction of water during wetting–drying transitions without generating destructive capillary stresses at the coating–fiber interface, in contrast to dense monolithic absorbers, where repeated swelling can drive crack propagation and delamination (AlMallahi et al., 2025). The 94% retention substantially exceeds the performance retention typically reported for unprotected MXene coatings on synthetic polymer-foam substrates.

Desalination Performance and Water Quality Assessment

Ionic Rejection Performance

The concentrations of Na^+, K^+, Ca^{2+}, and Mg^{2+} in the MC-CLS condensate collected from simulated seawater feed are presented in Fig. 11a alongside WHO maximum permissible limits. The post-desalination concentrations of all four ionic species in the condensate were dramatically reduced relative to the feed brine and were consistently well below the WHO limits of 200, 12, 300, and 50 mg L^{-1} for Na^+, K^+, Ca^{2+}, and Mg^{2+}, respectively. The Na^+ rejection performance is particularly notable given the high feed concentration in simulated seawater (~10,000 mg L^{-1} Na^+), yielding a rejection ratio

exceeding 98%. The exceptional ionic rejection arises from the inherent thermodynamic selectivity of the liquid-to-vapor phase transition process. During evaporation, water molecules enter the vapor phase as neutral H_2O vapor, which carries no ionic charge and excludes dissolved ions through an energetic barrier to co-evaporation. This mechanism is fundamentally different from and thermodynamically more robust than the size-exclusion or charge-repulsion mechanisms operative in pressure-driven membrane desalination, which are susceptible to solute transport through membrane defects and concentration polarization at high feed salinities (Moneer & Elewa, 2024). Consequently, the ionic rejection is non-selective in excluding species regardless of charge, ionic radius, or hydration energy, which explains the uniformly high rejection ratios observed for all four measured cations.

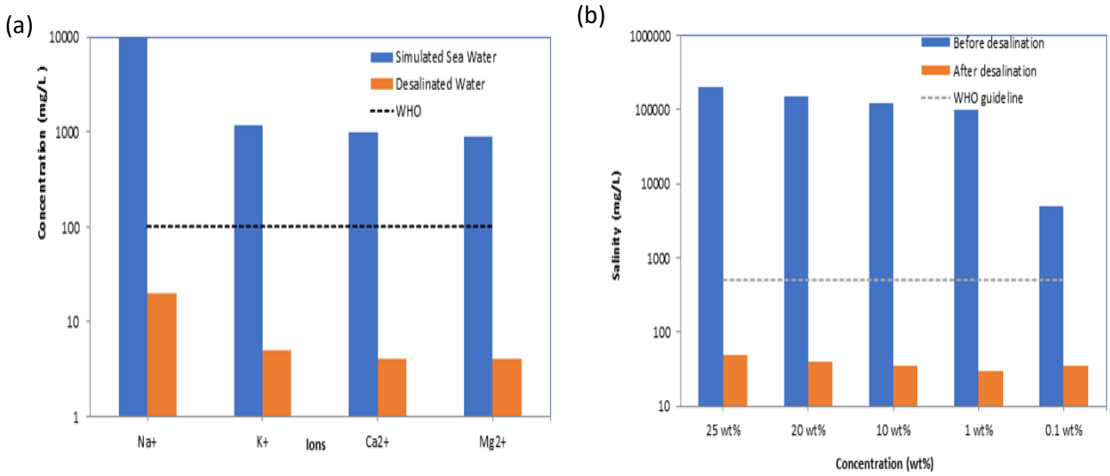


Figure 11. (a) Concentration of ions and (b) Salinity in different brine samples before and after desalination. The dashed line demoted the World Health Organization (WHO) standard of ions and salinity for drinking water.

Salinity Reduction and WHO Compliance

Figure 11b presents the salinity in the feed brine and condensate across a feed salinity range spanning from brackish water (~3,000 mg L^{-1}) to standard seawater (~35,000 mg L^{-1}), benchmarked against the WHO potable water salinity guideline of 600 mg L^{-1}. All condensate salinity values were consistently below the WHO threshold across the entire tested feed salinity range, confirming the practical utility of MC-CLS for the production of potable water from both brackish groundwater and seawater sources. Critically, the condensate quality was largely independent of feed salinity, which is a key operational advantage that distinguishes evaporation-condensation systems from pressure-driven

technologies. Because the evaporation mechanism operates on the vapor pressure of pure water (which is independent of the dissolved salt concentration within the relevant range) rather than on an osmotic pressure difference across a semi-permeable membrane, the driving force is not diminished at higher feed salinities, and the product water quality is not compromised by concentration polarization effects (Oraby et al., 2025). This feed-salinity independence represents a decisive thermodynamic advantage for deployment in environments with highly variable or extremely saline water sources, where membrane technologies are energetically prohibitive.

Conclusion

This study establishes a fully integrated and sustainable pathway spanning the energy-efficient synthesis of $Ti_3C_2T_x$ MXene from low-cost precursors to its application as an advanced photothermal material in solar desalination. The Ti_3AlC_2 MAX phase was successfully synthesized at 1100 °C via a molten salt-assisted (MS^3) route using TiO_2, Al, and activated carbon within a NaCl–KCl eutectic system, achieving a substantial reduction in the synthesis temperature compared to conventional methods. Structural and chemical analyses confirmed the high crystallinity and formation of characteristic layered structures, while subsequent selective etching enabled the successful conversion to $Ti_3C_2T_x$ MXene with a well-defined morphology and surface terminations conducive to photothermal applications.

The integration of $Ti_3C_2T_x$ onto a carbonized luffa sponge via dip coating resulted in a robust MC-CLS composite exhibiting near-unity broadband solar absorption, enhanced hydrophilicity, and improved thermal stability. Systematic optimization identified an absorber thickness of 12 mm as optimal, ensuring effective thermal localization while maintaining efficient, capillary-driven water transport. Under one-sun illumination, the system achieved a high evaporation rate and solar-to-steam conversion efficiency, with performance scaling proportionally with increased solar flux and demonstrating excellent durability over repeated operational cycles.

Importantly, the desalination performance was validated through ion rejection analysis, confirming a high salt removal efficiency and consistent production of potable water that meets international standards, irrespective of feed salinity. Overall, the findings highlight the strong potential of the MC-CLS system as a scalable and durable solar desalination platform, while also demonstrating the viability of the MS^3 route as an energy-

and cost-efficient strategy for MXene synthesis. Future investigations should focus on real-world deployment, system scale-up, long-term stability under outdoor conditions, and functional modifications to address fouling and broaden the applicability to complex wastewater streams.

Credit Author Contribution Statement

Mohammed Muktar Nono: Conceptualization, Methodology, Investigation, Formal analysis, Writing – Original Draft. Idris Misau Muhammad: Supervision, Resources, Writing – Review & Editing. Abdulrasheed A. Abdulrahman: Supervision, Writing – Review & Editing. Usman Dadum Hamza: Supervision, Writing – Review & Editing. Prashobh Karunakaran: Supervision, Writing – Review & Editing.

Declaration of Competing Interests

The authors declare no competing financial interests or personal relationships that could have appeared to influence the work reported in this paper.

Acknowledgements

The authors gratefully acknowledge the UTS-COMSTECH Research fellowship programme for laboratory access and supervisory support.

References

Abdullah, H., Shuwanto, H., Astarini, N. A., Lie, J., Ginting, R. T., Tsai, M.-L., Shih, S.-J., & Sillanpää, M. (2025). A brief review of emerging strategies in designing interfacial solar steam generation for desalination, water purification, power generation, and sea farming. *ACS Applied Energy Materials, 8*(5), 2663–2704. https://doi.org/10.1021/acsaem.4c03384

Alhabeb, M., Maleski, K., Anasori, B., Lelyukh, P., Clark, L., Sin, S., & Gogotsi, Y. (2017). Guidelines for synthesis and processing of two-dimensional titanium carbide (Ti3C2Tx MXene). *Chemistry of Materials, 29*(18), 7633–7644. https://doi.org/10.1021/acs.chemmater.7b02847

AlMallahi, M. N., Selim, M. Y. E., & Elgendi, M. (2025). Interfacial solar evaporation using biomass: Environmental impact, financial feasibility, and a bibliometric perspective. *Desalination, 614*, 119160. https://doi.org/10.1016/j.desal.2025.119160

Amani, A. M., Tayebi, L., Abbasi, M., Vaez, A., Kamyab, H., Chelliapan, S., & Vafa, E. (2024). The need for smart materials in an expanding smart world: MXene-based wearable electronics and their advantageous applications. *ACS Omega, 9*(3), 3123–3142. https://doi.org/10.1021/acsomega.3c06590

Boretti, A., & Rosa, L. (2019). Reassessing the projections of the World Water Development Report. *npj Clean Water, 2*(1), 15. https://doi.org/10.1038/s41545-019-0039-9

Bu, F., Zagho, M. M., Ibrahim, Y., Ma, B., Elzatahry, A., & Zhao, D. (2020). Porous MXenes: Synthesis, structures, and applications. *Nano Today, 30*, 100803. https://doi.org/10.1016/j.nantod.2019.100803

Chebbi, R. (2021). Absorption and spreading of a liquid droplet over a thick porous substrate. *ACS Omega, 6*(7), 4649–4655. https://doi.org/10.1021/acsomega.0c05341

Chen, L., Mu, X., Guo, Y., Lu, H., Yang, Y., Xiao, C., & Hasi, Q. (2022). MXene-doped kapok fiber aerogels with oleophobicity for efficient interfacial solar steam generation. *Journal of Colloid and Interface Science, 626*, 35–46. https://doi.org/10.1016/j.jcis.2022.06.143

Dash, A., Vaßen, R., Guillon, O., & Gonzalez-Julian, J. (2019). Molten salt shielded synthesis of oxidation-prone materials in air. *Nature Materials, 18*(5), 465–470. https://doi.org/10.1038/s41563-019-0328-1

Dillon, A. D., Ghidiu, M. J., Krick, A. L., Griggs, J., May, S. J., Gogotsi, Y., Barsoum, M. W., & Fafarman, A. T. (2016). Highly conductive optical quality solution-processed films of 2D titanium carbide. *Advanced Functional Materials, 26*(23), 4162–4168. https://doi.org/10.1002/adfm.201600357

Farabi, S. N., Habib, K., Mim, M., Zaed, M. A., Ali, S. A., Younas, M., & Saidur, R. (2024). The future of solar-driven interfacial steam generation for sustainable water desalination: Drivers, challenges, and opportunities—Review. *Results in Engineering, 23*, 102649. https://doi.org/10.1016/j.rineng.2024.102649

Gao, M., Zhu, L., Peh, C. K. N., & Ho, G. W. (2019). Solar absorber material and system designs for photothermal water vaporization towards clean water and energy production. *Energy & Environmental Science, 12*(3), 841–864. https://doi.org/10.1039/C8EE01146J

Ghidiu, M., Lukatskaya, M. R., Zhao, M.-Q., Gogotsi, Y., & Barsoum, M. W. (2014). Conductive two-dimensional titanium carbide "clay" with high volumetric capacitance. *Nature, 516*(7529), 78–81. https://doi.org/10.1038/nature13970

Ginting, R. T., Abdullah, H., & Fauzia, V. (2022). Facile preparation of MXene and protonated-g-C3N4 on natural latex foam for highly efficient solar steam generation. *Materials Letters, 313*, 131779. https://doi.org/10.1016/j.matlet.2022.131779

Gogotsi, Y., & Anasori, B. (2019). The rise of MXenes. *ACS Nano, 13*(8), 8491–8494. https://doi.org/10.1021/acsnano.9b06394

Gogotsi, Y., & Huang, Q. (2021). MXenes: Two-dimensional building blocks for future materials and devices. *ACS Nano, 15*(4), 5775–5780. https://doi.org/10.1021/acsnano.1c03161

Halim, J., Lukatskaya, M. R., Cook, K. M., Lu, J., Smith, C. R., Näslund, L.-Å., May, S. J., Hultman, L., Gogotsi, Y., Eklund, P., & Barsoum, M. W. (2014). Transparent conductive two-dimensional titanium carbide epitaxial thin films. *Chemistry of Materials, 26*(7), 2374–2381. https://doi.org/10.1021/cm500641a

Hao, S., Han, H., Yang, Z., Chen, M., Jiang, Y., Lu, G., Dong, L., Wen, H., Li, H., Liu, J., Wu, L., Wang, Z., & Wang, F. (2022). Recent advancements on photothermal conversion and antibacterial applications over MXenes-based materials. *Nano-Micro Letters, 14*(1), 178. https://doi.org/10.1007/s40820-022-00901-w

Huang, Y., Tian, K., Zhang, C., Wang, J., Shu, R., Chen, Z., Liu, X., Li, Y., & Xu, L. (2023). Lightweight and efficient luffa sponge carbon/Co composites with adjustable electromagnetic wave absorption properties. *Journal of Colloid and Interface Science, 652*, 1138–1147. https://doi.org/10.1016/j.jcis.2023.08.147

Ingrao, C., Strippoli, R., Lagioia, G., & Huisingh, D. (2023). Water scarcity in agriculture: An overview of causes, impacts and approaches for reducing the risks. *Heliyon, 9*(8), e18507. https://doi.org/10.1016/j.heliyon.2023.e18507

Jolly, S., Paranthaman, M. P., & Naguib, M. (2021). Synthesis of Ti3C2Tz MXene from low-cost and environmentally friendly precursors. *Materials Today Advances, 10*, 100139. https://doi.org/10.1016/j.mtadv.2021.100139

Li, C., Wang, L., & Zhang, L. (2024). A case study in natural fibre material (luffa sponge) development using E2-material-driven design. *Sustainability, 16*(8), 3490. https://doi.org/10.3390/su16083490

Li, K., Chang, T.-H., Li, Z., Yang, H., Fu, F., Li, T., Ho, J. S., & Chen, P.-Y. (2019). Biomimetic MXene textures with enhanced light-to-heat conversion for solar steam generation and wearable thermal management. *Advanced Energy Materials, 9*(34), 1901687. https://doi.org/10.1002/aenm.201901687

Li, R., Zhang, L., Shi, L., & Wang, P. (2017). MXene Ti3C2: An effective 2D light-to-heat conversion material. *ACS Nano, 11*(4), 3752–3759. https://doi.org/10.1021/acsnano.6b08415

Liu, A., Yang, Q., Ren, X., Meng, F., Gao, L., Gao, M., Yang, Y., Ma, T., & Wu, G. (2020). Energy- and cost-efficient NaCl-assisted synthesis of MAX-phase Ti3AlC2 at lower temperature. *Ceramics International, 46*(5), 6934–6939. https://doi.org/10.1016/j.ceramint.2019.11.008

Liu, C., Hong, K., Sun, X., Natan, A., Luan, P., Yang, Y., & Zhu, H. (2020). An "antifouling" porous loofah sponge with internal microchannels as solar absorbers and water pumpers for thermal desalination. *Journal of Materials Chemistry A, 8*(25), 12323–12333. https://doi.org/10.1039/D0TA03872E

Liu, Y., Wu, K., Lu, M., Jiao, E., Zhang, H., Shi, J., & Lu, M. (2021). Highly thermal conductivity and flame retardant flexible graphene/MXene paper based on an optimized interface and nacre laminated structure. *Composites Part A: Applied Science and Manufacturing, 141*, 106227. https://doi.org/10.1016/j.compositesa.2020.106227

Ma, Y.-Y., Wu, C.-X., Feng, X.-J., Tan, H.-Q., Yan, L.-K., Liu, Y., Kang, Z.-H., Wang, E.-B., & Li, Y.-G. (2017). Highly efficient hydrogen evolution from seawater by a low-cost and stable CoMoP@C electrocatalyst superior to Pt/C. *Energy & Environmental Science, 10*(3), 788–798. https://doi.org/10.1039/C6EE03768B

Masekela, D., Mafa, P. J., Yusuf, T. L., Balogun, S. A., Kuvarega, A. T., & Modibane, K. D. (2026). Recent advances in MXene-based nanocomposites for photocatalytic wastewater treatment, carbon dioxide reduction, and hydrogen production: A comprehensive review. *Coordination Chemistry Reviews, 549*, 217270. https://doi.org/10.1016/j.ccr.2025.217270

Moneer, A. A., & Elewa, M. M. (2024). The innovative technologies for desalination and their cost benefits. *Egyptian Journal of Aquatic Research, 50*(4), 431–446. https://doi.org/10.1016/j.ejar.2024.11.008

Oraby, H., Ezz, A. A., & Hegazy, G. E. (2025). Advances in desalination: Pioneering methods and the future of water sustainability. *Discover Water, 5*(1), 88. https://doi.org/10.1007/s43832-025-00222-0

Parker, T., Zhang, D., Bugallo, D., Shevchuk, K., Downes, M., Valurouthu, G., Inman, A., Chacon, B., Zhang, T., Shuck, C. E., Hu, Y.-J., & Gogotsi, Y. (2024). Fourier-transform infrared spectral library of MXenes. *Chemistry of Materials, 36*(17), 8437–8446. https://doi.org/10.1021/acs.chemmater.4c01536

Protyai, M. I. H., & Rashid, A. B. (2024). A comprehensive overview of recent progress in MXene-based polymer composites: Their fabrication processes, advanced applications, and prospects. *Heliyon, 10*(17), e37030. https://doi.org/10.1016/j.heliyon.2024.e37030

Rasool, K., Pandey, R. P., Rasheed, P. A., Buczek, S., Gogotsi, Y., & Mahmoud, K. A. (2019). Water treatment and environmental remediation applications of two-dimensional metal carbides (MXenes). *Materials Today, 30*, 80–102. https://doi.org/10.1016/j.mattod.2019.05.017

Shafaee, M., & Goharshadi, E. K. (2025). Photothermal materials—Solar-to-heat conversion phenomena. In J. M. Gohil & K. Dutta (Eds.), *Photothermal materials and membranes for solar-driven water treatment* (pp. 37–81). Elsevier. https://doi.org/10.1016/B978-0-443-21788-3.00002-0

Shekhirev, M., Shuck, C. E., Sarycheva, A., & Gogotsi, Y. (2021). Characterization of MXenes at every step, from their precursors to single flakes and assembled films. *Progress in Materials Science, 120*, 100757. https://doi.org/10.1016/j.pmatsci.2020.100757

Shokri, A., & Fard, M. S. (2022). A sustainable approach in water desalination with the integration of renewable energy sources: Environmental engineering challenges and perspectives. *Environmental Advances, 9*, 100281. https://doi.org/10.1016/j.envadv.2022.100281

Shuck, C. E., Sarycheva, A., Anayee, M., Levitt, A., Zhu, Y., Uzun, S., Balitskiy, V., Zahorodna, V., Gogotsi, O., & Gogotsi, Y. (2020). Scalable synthesis of Ti3C2Tx MXene. *Advanced Engineering Materials, 22*(3), 1901241. https://doi.org/10.1002/adem.201901241

Soman, S., Kulkarni, S., Pandey, A., Dhas, N., Shirur, K. S., Gude, R. S., Vidya, S. M., Nayak, S., George, S. D., & Mutalik, S. (2024). Unlocking the power of MXenes—Crafting a 2D nanoplatform for tomorrow: Synthesis, functionalization, stability, and biomedical applications. *Materials Today Communications, 38*, 107711. https://doi.org/10.1016/j.mtcomm.2023.107711

Tayeh, Y. A. (2024). A comprehensive review of reverse osmosis desalination: Technology, water sources, membrane processes, fouling, and cleaning. *Desalination and Water Treatment, 320*, 100882. https://doi.org/10.1016/j.dwt.2024.100882

Thomas, S. A., Cherusseri, J., & Rajendran, D. N. (2025). Loofah sponge: A sustainable material for wastewater desalination. *RSC Sustainability, 3*(7), 2806–2832. https://doi.org/10.1039/D5SU00043B

Wang, Y., Qi, Q., Fan, J., Wang, W., & Yu, D. (2021). Simple and robust MXene/carbon nanotubes/cotton fabrics for textile wastewater purification via solar-driven

interfacial water evaporation. *Separation and Purification Technology, 254*, 117615. https://doi.org/10.1016/j.seppur.2020.117615

Wilson, H. M., Pandit, T. P., A. R., S. R., Thirugnanasambantham, A. K., Lim, H. W., & Lee, S. J. (2025). Engineering electrothermally enhanced interfacial evaporation for high-performance solar desalination. *Communications Engineering, 4*(1), 166. https://doi.org/10.1038/s44172-025-00498-z

Wu, J., Zhang, T., Qu, J., Jiao, F.-Z., Hu, C., Zhao, H.-Y., Li, X., & Yu, Z.-Z. (2023). Hydrothermally modified 3D porous loofah sponges with MoS2 sheets and carbon particles for efficient solar steam generation and seawater desalination. *ACS Applied Materials & Interfaces, 15*(24), 29457–29467. https://doi.org/10.1021/acsami.3c05198

Wu, X., Lu, Y., Ren, X., Wu, P., Chu, D., Yang, X., & Xu, H. (2024). Interfacial solar evaporation: From fundamental research to applications. *Advanced Materials, 36*(23), 2313090. https://doi.org/10.1002/adma.202313090

Yang, L. X., Wang, Y., Zhang, H. L., Liu, H. J., & Zeng, C. L. (2019). A simple method for the synthesis of nanosized Ti3AlC2 powder in NaCl–KCl molten salt. *Materials Research Letters, 7*(9), 361–367. https://doi.org/10.1080/21663831.2019.1613695

Yao, W., Zhu, X., Xu, Z., Davis, R. A., Liu, G., Zhong, H., Lin, X., Dong, P., Ye, M., & Shen, J. (2022). Loofah sponge-derived hygroscopic photothermal absorber for all-weather atmospheric water harvesting. *ACS Applied Materials & Interfaces, 14*(3), 4680–4689. https://doi.org/10.1021/acsami.1c20576

Yu, Z., & Wu, P. (2020). Biomimetic MXene-polyvinyl alcohol composite hydrogel with vertically aligned channels for highly efficient solar steam generation. *Advanced Materials Technologies, 5*(6), 2000065. https://doi.org/10.1002/admt.202000065

Zaed, M. A., Tan, K. H., Saidur, R., Pandey, A. K., & Cherusseri, J. (2024). Low-cost synthesis of Ti3C2Tx MXene-based sponge for solar steam generation and clean water production. *Ceramics International, 50*(16), 27910–27922. https://doi.org/10.1016/j.ceramint.2024.05.086

Zhang, Q., Yi, G., Fu, Z., Yu, H., Chen, S., & Quan, X. (2019). Vertically aligned Janus MXene-based aerogels for solar desalination with high efficiency and salt resistance. *ACS Nano, 13*(11), 13196–13207. https://doi.org/10.1021/acsnano.9b06180

Zhao, H.-Y., Huang, J., Zhou, J., Chen, L.-F., Wang, C., Bai, Y., Zhou, J., Deng, Y., Dong, W.-X., Li, Y.-S., & Yu, S.-H. (2022). Biomimetic design of macroporous 3D truss materials for efficient interfacial solar steam generation. *ACS Nano, 16*(3), 3554–3562. https://doi.org/10.1021/acsnano.1c10184

Zhou, H., Wang, S., Cao, H., Zhou, M., Wang, H., Xian, P., He, X., Fu, J., & Liu, J. (2025). A multifunctional biomass-derived solar evaporator constructed from Chinese medicine residues for cost-effective solar evaporation. *Separation and Purification Technology, 377*, 134491. https://doi.org/10.1016/j.seppur.2025.134491